

Local Structure of Mott Insulating Iron Oxychalcogenides $\text{La}_2\text{O}_2\text{Fe}_2\text{OM}_2$ ($M = \text{S}, \text{Se}$)

B. Karki,¹ A. Alfailakawi,¹ Benjamin A. Frandsen,^{2,3} M. S. Everett,⁴ J. C. Neufeind,⁴ Binjie Xu,⁵ Hangdong Wang,⁵ Minghu Fang,^{5,6} and B. Freelon^{1,7*}

¹*Department of Physics, University of Louisville, Louisville, Kentucky 40208, USA*

²*Materials Science Division, Lawrence Berkeley National Laboratory, Berkeley, California 94720, USA*

³*Department of Physics and Astronomy, Brigham Young University, Provo, Utah 84602, USA*

⁴*Spallation Neutron Source, Oak Ridge National Laboratory, Oak Ridge, Tennessee 37831, United States*

⁵*Department of Physics, Zhejiang University, Hangzhou 310027, China*

⁶*Collaborative Innovation Center of Advanced Microstructures, Nanjing University, Nanjing 210093, China*

⁷*Department of Physics and Texas Center for Superconductivity, University of Houston, Texas 77204, USA*

(Dated: July 6, 2021)

We describe the local structural properties of the iron oxychalcogenides, $\text{La}_2\text{O}_2\text{Fe}_2\text{OM}_2$ ($M = \text{S}, \text{Se}$), by using pair distribution function (PDF) analysis applied to total scattering data. Our results of neutron powder diffraction show that $M = \text{S}$ and Se possess similar nuclear structure at low and room temperatures. The local crystal structures were studied by investigating deviations in atomic positions and the extent of the formation of orthorhombicity. Analysis of the total scattering data suggests that buckling of the Fe_2O plane occurs below 100 K. The buckling may occur concomitantly with a change in octahedral height. Furthermore, within a typical range of 1-2 nm, we observed short-range orthorhombic-like structure suggestive of nematic fluctuations in both of these materials.

I. INTRODUCTION

Iron-based superconductors (FeSCs) has attracted a large amount of attention due to the high transition temperature T_c at which they become superconducting. Although the precise pairing mechanism in these materials remains unknown, it is thought that electron-electron interactions play an important role. Such unconventional superconductivity is in contrast to the conventional electron-phonon coupling [1, 2] present in BCS superconductors. In order to examine the strong-Coulombic postulate for Fe pnictides and chalcogenides, studies were conducted [3–8] to find iron-based Mott insulators that could be driven into the superconducting phase [9, 10]. The iron oxychalcogenides $\text{La}_2\text{O}_2\text{Fe}_2\text{OM}_2$ ($M = \text{S}, \text{Se}$) emerged as a candidate material because they are Mott insulators with structural similarities to the iron pnictides. Several attempts to induce SC in $\text{La}_2\text{O}_2\text{Fe}_2\text{O}(\text{S}, \text{Se})_2$ have been made; however, to date, there are no published reports of SC in these systems [11]. Nevertheless, studying non-superconducting Mott insulators such as $\text{La}_2\text{O}_2\text{Fe}_2\text{OM}_2$ can enhance our understanding of the Mott insulating region of the iron-chalcogenide electronic phase diagram [1].

Studying the Mott insulating phase in iron oxychalcogenides might enhance our understanding of the strongly correlated scenarios that lead to high temperature superconductivity [12]. Superconductivity in the cuprate superconductors is based on an electron or hole doping of a strongly correlated, Mott insulating phase [13]. Hole-doped cuprates are prone to a variety of different type of electronic ordering like charge ordering and nematic ordering [14]. The electronic nematicity breaks rotational symmetry while preserving the translational symmetry; this phase has been observed in the iron-based superconductors.

The iron oxychalcogenides $\text{La}_2\text{O}_2\text{Fe}_2\text{OM}_2$ were first reported as antiferromagnetic (AFM) by Mayer et. al. [15]. This layered mixed anion material consists of a body-centered tetragonal crystal structure ($I4/mmm$) with fluorite-like $[\text{La}_2\text{O}_2]^{2+}$ layers and $[\text{Fe}_2\text{O}]^{2+}$ sheets separated by M^{2-} anions [16]. In this structure, $[\text{Fe}_2\text{O}]^{2+}$ consists of an anti- CuO_2 arrangement with an Fe^{2+} cation coordinated by four M^{2-} (above and below the plane) and two in-plane oxygen atoms, forming a tilted Fe-centered FeO_2Se_4 octahedron [12, 15, 17–20]. Fig. 1 shows the crystal structure of $\text{La}_2\text{O}_2\text{Fe}_2\text{OM}_2$ and its octahedra. While an antiferromagnetic ordering was observed at Néel temperatures T_N of 107.2 K and 90.1 K for $\text{La}_2\text{O}_2\text{Fe}_2\text{OS}_2$ and $\text{La}_2\text{O}_2\text{Fe}_2\text{OSe}_2$, respectively [16], structural studies using X-ray [19] and neutron [16] powder diffraction studies did not observe a structural phase transition in $\text{La}_2\text{O}_2\text{Fe}_2\text{O}(\text{S}, \text{Se})_2$. Inelastic neutron scattering (INS) experiments have indicated the AFM order to be consistent with a 2 - k magnetic structure in which two spin stripe phases are oriented 90° with respect to each other. [16, 17, 21, 22]

Therefore, the structural and magnetic behavior do not have a similar correspondence that is observed in some iron-pnictides and iron-chalcogenides in which the mag-

* bkgreelon@uh.edu; Notice: This manuscript has been authored by UT-Battelle, LLC, under contract DE-AC05-00OR22725 with the US Department of Energy (DOE). The US government retains and the publisher, by accepting the article for publication, acknowledges that the US government retains a nonexclusive, paid-up, irrevocable, worldwide license to publish or reproduce the published form of this manuscript, or allow others to do so, for US government purposes. DOE will provide public access to these results of federally sponsored research in accordance with the DOE Public Access Plan (<http://energy.gov/downloads/doe-public-access-plan>).

netic and structural phase transitions are in very close proximity. The absence of a structural phase transition in the $\text{La}_2\text{O}_2\text{Fe}_2\text{O}(\text{S}, \text{Se})_2$ Mott insulators motivates us to study the local structure to determine whether their short-range lattice symmetries undergo changes at the magnetic transitions. In particular, we are interested in understanding whether local deviations from the average tetragonal structure occur and we seek to characterize lattice correlations with physical properties.

To date, several studies of FeSCs [23–28] have revealed the presence of a long-range, non-superconducting state called the nematic phase [24] that precedes the superconducting phase transition. The long-range nematic phase, which has been observed in both iron pnictides and iron chalcogenides, develops at a structural phase transition temperature T_s higher than a magnetic transition temperature T_N [29]. The long-range nematic ordering is manifested by spontaneous rotational symmetry breaking while the translational symmetry is preserved [30, 31]. In iron pnictide superconductors symmetry is broken between x and y directions in the Fe-plane [24]. This reduces the rotational point group symmetry from tetragonal to orthorhombic while preserving the translational symmetry. [28, 30]. A hallmark feature of the nematic phase in the FeSCs is the presence of large anisotropies of electronic properties, such as the resistivity, along the x and y directions. These anisotropies are larger than would be expected from the magnitude of the structural distortion alone, indicating that the nematic instability exists in the electronic system, while the structural symmetry breaking is simply a consequence of the underlying electronic symmetry breaking. Similar electronic nematicity has also been observed in other electron fluids such as those observed in the cuprates or quantum Hall systems [28, 32]. This electronic nematicity is related to, but distinct from, other types of nematicity, such as the original use of the term to describe the directional alignment of molecules in liquid crystals [32], or a purely structural nematic order that is unrelated to any instabilities of an electron fluid.

In the case of FeSCs, the nematic state is suppressed upon doping, and superconductivity eventually emerges out of the nematic phase [33, 34]. Sometimes, nematic ordering persists into the superconducting state, as in LiFeAs [35]. The origin of the electronic nematic ordering is not yet fully understood. In the pnictides, it appears to be related to the magnetism, but this may not be the case in iron-chalcogenides such as FeSe , which does not show long-range magnetic ordering [29].

Recently, the pair distribution function (PDF) technique [36, 37] has been used to study the local atomic arrangement and structural fluctuations frequently associated with nematic fluctuations in iron-based superconductors for both normal and superconducting phases. PDF methods can be used to measure local scale deviations from the global crystal symmetry of a material [24, 38]. In $\text{FeSe}_{1-x}\text{Te}_x$ systems, PDF investigated the reduction of local crystal symmetry which en-

hances the local moment formation leading to magnetic instability [39]. X-ray and neutron PDF on FeSe and $(\text{Sr}, \text{Na})\text{Fe}_2\text{As}_2$ revealed the presence of short-range orthorhombic distortions at temperatures well above the static nematic and orthorhombic ordering temperature T_s [30, 31, 34, 38]. These short-range orthorhombic fluctuations of the structure were interpreted as consequences of fluctuations of the underlying electronic nematic phase. The observation of structural nematic fluctuations in iron-based superconductors, by using neutron and x-ray PDF analysis, provided evidence that nematic degrees of freedom exist near the superconducting phase [30]. PDF analysis has also been used by Horigane et. al [40] to probe the local structure of $\text{La}_2\text{O}_2\text{Fe}_2\text{OS}_2$ and found a large anisotropic thermal displacement parameter for the O(2) atom along the c -axis (U_{33}). That study concluded that the crystal structure is strongly coupled to the magnetism in this system.

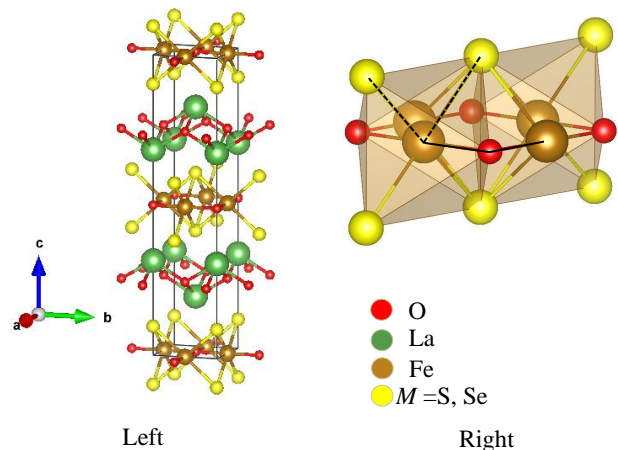


FIG. 1. The crystal structure of $\text{La}_2\text{O}_2\text{Fe}_2\text{OM}_2$ ($M = \text{S}, \text{Se}$) is shown in the left panel. The right panel shows FeO_2Se_4 octahedra, where the Fe atom is surrounded by four $M = \text{S}, \text{Se}$ atoms and two O(2) atoms. Black solid lines show the angle formed by Fe-O-Fe atoms while the dashed lines show $M\text{-Fe-M}$ angle.

In this work, we report the use of the neutron pair distribution function (PDF) technique to study the local structure of $\text{La}_2\text{O}_2\text{Fe}_2\text{O}(\text{S}, \text{Se})_2$. The experimental methods are discussed in Section II, the results of this study are presented in Section III, section IV includes the discussion and the conclusions are presented in section V. Our results indicate the presence of short-range orthorhombic distortions suggestive of short-range nematicity in both materials $\text{La}_2\text{O}_2\text{Fe}_2\text{O}(\text{S}, \text{Se})_2$, despite the persistence of tetragonal symmetry in the average structure at all temperatures. We discuss the behavior of these fluctuations as a function of temperature. It appears that the change in the chalcogen, from S to Se, does not affect this behavior.

II. EXPERIMENTAL METHODS

1. Synthesis

$\text{La}_2\text{O}_2\text{Fe}_2\text{O}(\text{S}, \text{Se})_2$ samples were prepared by a solid-state reaction method [15] from stoichiometric amounts of high purity La_2O_3 , S, Se, and Fe powders. The appropriate mixture of these powders was grounded thoroughly, pelletized then heated in an evacuated quartz tube at 1030°C for 72 hours. This process was repeated three times. After being pulverized into fine powders, lab-based x-ray powder diffraction showed the materials to be of the high-quality and single phase [12, 15, 16].

2. Neutron Powder Diffraction

Time-of-flight (TOF) neutron powder diffraction measurements were performed at the POWGEN diffractometer of the Spallation Neutron Source (SNS) at Oak Ridge National Laboratory (ORNL). Five grams of $\text{La}_2\text{O}_2\text{Fe}_2\text{OS}_2$ and 4.5 g of $\text{La}_2\text{O}_2\text{Fe}_2\text{OSe}_2$ powders were placed in vanadium cans. Room temperature (300 K) measurement were performed, on each sample, for approximately one hour. The center wavelength and d -spacing range of neutrons in this experiment were 1.5 Å and 0.49664-13.50203 Å respectively. Rietveld refinements were conducted using GSAS-II software [41].

3. Pair Distribution Function

Neutron total scattering data were collected using the Nano-scale Ordered Materials Diffractometer (NOMAD) beamline at the SNS in ORNL. $\text{La}_2\text{O}_2\text{Fe}_2\text{O}(\text{S}, \text{Se})_2$ powders were loaded and sealed in the vanadium cans inside a glove-box and were placed in an orange cryostat. A total of sixteen measurements were performed on each sample at various temperatures ranging from 2 K to 300 K. A higher number of data points were taken, in small steps, around the Néel temperature. Data were collected for approximately two hours at each temperature. In order to obtain structural information relevant to the samples, an empty vanadium sample can was measured for two hours for background subtraction.

The reduced pair distribution function (PDF) $G(r)$ is obtained experimentally by Fourier transforming the total scattering data as follows:

$$G(r) = \frac{2}{\pi} \int_{Q_{min}}^{Q_{max}} Q(S(Q) - 1) \sin(Qr) dQ, \quad (1)$$

Where $S(Q)$ is the normalized structure factor, and Q is the scattering vector, defined as $Q = \frac{4\pi \sin(\theta)}{\lambda}$ in which λ and θ are the neutron wavelength and scattering angle, respectively. PDF data were refined and analyzed using PDFGUI [37] program and DIFFPY-CMI [42] suite. For the PDF analysis, values for Q_{min} and Q_{max} were 0.1 Å

and 31.4 Å respectively. The calculated reduced pair distribution function $G_c(r)$ is obtained from the structural model using equation (2) [43].

$$G_c(r) = \frac{1}{r} \sum_i \sum_j \left[\left(\frac{b_i b_j}{\langle b \rangle^2} \right) \delta(r - r_{ij}) \right] - 4\pi r \rho_0 \quad (2)$$

where b_i , b_j and $\langle b \rangle$ are the average scattering power of constituent atoms of the sample. The summation is over all atoms i and j in the model, where the distance separating any given pair of atoms is r_{ij} .

III. RESULTS

A. Average and Local Structure

We confirmed the crystal structure of our samples through the neutron powder diffraction. The Rietveld refinement of neutron powder diffraction data was performed using GSAS II software [41]. Fig. 2(a) and (b) show the Rietveld refinement of neutron powder diffraction data measured at 300 K using neutrons of central wavelength 1.5 Å. Both $M = \text{S}, \text{Se}$ materials show similar nuclear structures having space group $I4/mmm$ (space group No. 139) which is consistent with the previous studies [15, 16]. Our findings show that the lattice parameters of $\text{La}_2\text{O}_2\text{Fe}_2\text{OSe}_2$ ($a = 4.0887(5)$ Å, $c = 18.6081(3)$ Å) is larger than that of the $\text{La}_2\text{O}_2\text{Fe}_2\text{OS}_2$ ($a = 4.0439(9)$ Å, $c = 17.8945(6)$ Å), as expected for the larger Se atoms. Rietveld refinement parameters of both $M = \text{S}, \text{Se}$ are tabulated in Table I including lattice parameters (a and c) as well as the anisotropic thermal displacement parameters U_{33} for all atoms. It was observed that U_{33} for O(2) site is much larger than all the other sites. For completeness Table II presents the atomic positions of constituents $\text{La}_2\text{O}_2\text{Fe}_2\text{OM}_2$ ($M = \text{S}, \text{Se}$) with their respective Wyckoff symbols and occupancies. The quality of the presented fits was characterized by the listed Rietveld parameters: R -whole pattern R_w , crystallographic factor R_F and goodness of fit tabulated in Table I.

Having obtained a confirmation of the global lattice symmetry for our samples, we then investigated the local symmetry [30, 34, 44–47]. The local structure data of $\text{La}_2\text{O}_2\text{Fe}_2\text{OM}_2$ ($M = \text{S}, \text{Se}$) was analyzed by using the PDF refinement program PDFGUI [37] to determine the lattice parameters, scale factor, atomic positions, and the thermal parameters. In order to allow for local orthorhombic symmetry breaking, we parameterized the lattice constants as $a = a_{mid}(1 + \delta)$ and $b = a_{mid}(1 - \delta)$, where $a_{mid} = \frac{a+b}{2}$ and $\delta = \left| \frac{a-b}{a+b} \right|$. The orthorhombicity parameter, δ was refined with a pseudo-orthorhombic model while in tetragonal model δ is 0 as lattice parameter a and b were equal. All refinements were performed on the Nyquist grid. Instrumental parameters q_{damp} and q_{broad} , which are the parameters that cor-

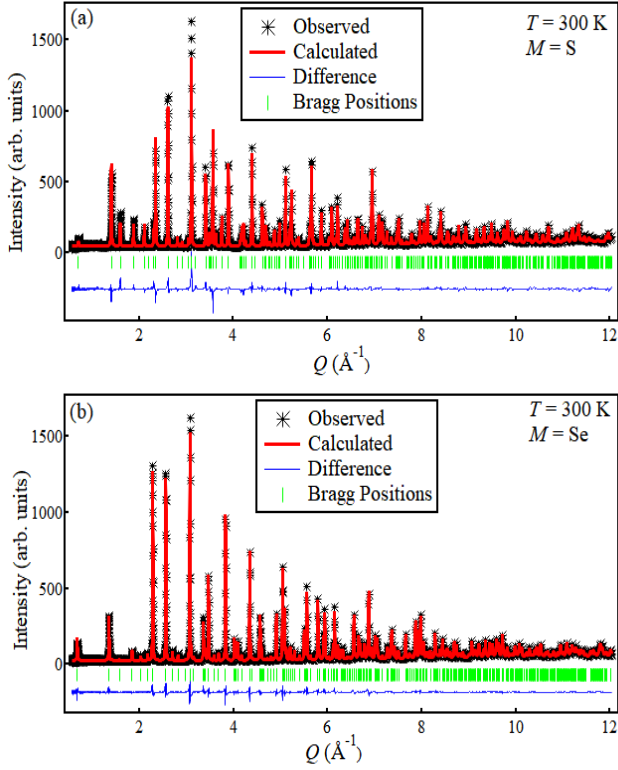


FIG. 2. Neutron Rietveld refinement of the nuclear model of a) $M = S$ and b) $M = Se$ at 300 K as a function of momentum transfer Q . The details of the fit are provided in the text.

	$La_2O_2Fe_2OSe_2$	$La_2O_2Fe_2OS_2$
a (Å)	4.0887(5)	4.0439(9)
c (Å)	18.6081(3)	17.8945(6)
La - U_{11} (Å ²)	0.0028(8)	0.00123(9)
Fe - U_{11} (Å ²)	0.0065(4)	0.00729(5)
O(1) - U_{11} (Å ²)	0.0038(4)	0.00013(4)
O(2) - U_{11} (Å ²)	0.0037(7)	0.00510(6)
M - U_{11} (Å ²)	0.0066(3)	0.00319(8)
La - U_{33} (Å ²)	0.00722(5)	0.01718(6)
Fe - U_{33} (Å ²)	0.01077(5)	0.02258(8)
O(1) - U_{33} (Å ²)	0.00998(8)	0.02049(9)
O(2) - U_{33} (Å ²)	0.02226(9)	0.04643(5)
M - U_{33} (Å ²)	0.00522(5)	0.02124(9)
Volume (Å ³)	311.08(8)	292.64(1)
Space Group	I_4/mmm	I_4/mmm
R_w (%)	6.74	6.79
R_F (%)	2.71	6.57
Goodness of fit	4.73	6.57

TABLE I. Refined parameters from Rietveld analysis of neutron powder diffraction data of $La_2O_2Fe_2O(S, Se)_2$ at $T = 300$ K.

rect the PDF envelope function [48, 49] for the instrument resolution [37, 43], were fixed by using an independent measurement of a standard Si sample. A direct comparison of quality of fit parameters of pseudo-orthorhombic symmetry and tetragonal symmetry PDF

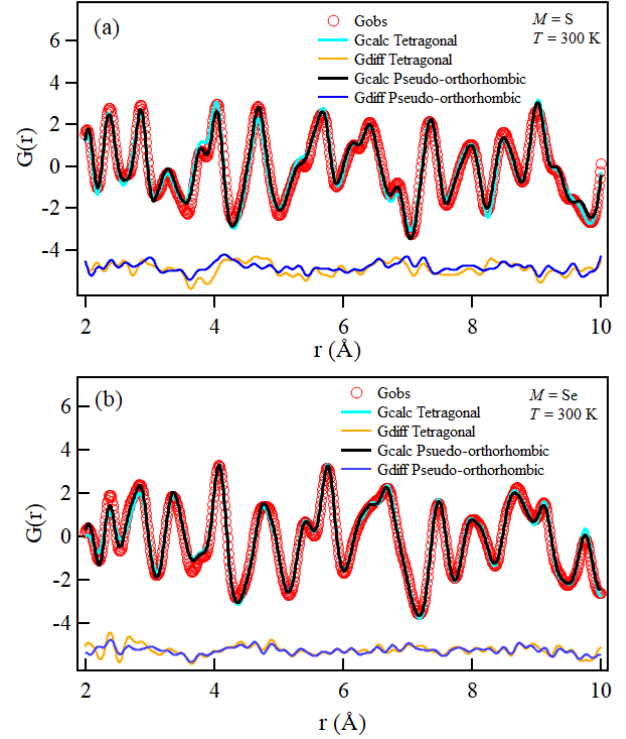


FIG. 3. Room temperature PDF fits of a) $M = S$ and b) $M = Se$ fitted with both tetragonal and pseudo-orthorhombic model within the range of $1.8 \text{ \AA} \leq r \leq 10.0 \text{ \AA}$.

fits of room temperature data of $La_2O_2Fe_2OM_2$ ($M = S, Se$) is shown in Table III and Fig. 3. It is clear that pseudo-orthorhombic model provides a significant improvement to the fit over the tetragonal model. This suggests that the local structure undergoes short-range orthorhombic distortions, while the average structure captured by Rietveld refinement against the Bragg peaks is purely tetragonal.

The lattice constants were obtained as a function of temperature using PDF analysis. Fig. 4 shows the temperature dependence of the lattice parameters a and c for both $La_2O_2Fe_2O(S, Se)_2$ samples in the range of 1.8 to 49.99 Å, where the Einstein model was superimposed to such obtained $a(T)$ and $c(T)$ dependencies. Following previous work [19], the Einstein fitting model was calculated using equations (3) and (4) under the assumption that the thermal expansion is proportional to the internal energy of a quantum mechanical oscillator [50]. Fig. 4 also shows that the lattice parameter a increases with increasing temperature and fits well with the Einstein model of thermal expansion [50]. However, the lattice parameter c shows a kink near 90 K in the case of $M = Se$ (see discussion).

$$a(T) = a_0 \left[1 + \alpha \theta_E f_E \left(\frac{\theta_E}{T} \right) \right] \quad (3)$$

La ₂ O ₂ Fe ₂ OSe ₂						La ₂ O ₂ Fe ₂ OS ₂					
Atom	Site	Occupancy	x	y	z	Atom	Site	Occupancy	x	y	z
La	4e	0.97(5)	0.5000	0.5000	0.1845(6)	La	4e	0.94(7)	0.5000	0.5000	0.1806(7)
Fe	4c	0.94(5)	0.5000	0.0000	0.0000	Fe	4c	0.92(7)	0.5000	0.0000	0.0000
Se	4e	0.95(6)	0.0000	0.0000	0.0963(6)	S	4c	0.92(8)	0.0000	0.0000	0.0945(13)
O1	4d	0.98(6)	0.5000	0.0000	0.2500	O1	4d	0.94(9)	0.5000	0.0000	0.2500
O2	2b	0.97(7)	0.5000	0.5000	0.0000	O2	2b	0.96(6)	0.5000	0.5000	0.0000

TABLE II. Atomic site, occupancy and fractional atomic coordinates of La₂O₂Fe₂O(S, Se)₂ at $T = 300$ K extracted from Rietveld analysis.

	La ₂ O ₂ Fe ₂ OSe ₂		La ₂ O ₂ Fe ₂ OS ₂	
	Pseudo-Orthorhombic	Tetragonal	Pseudo-Orthorhombic	Tetragonal
χ^2	24.20	43.77	41.45	74.13
Reduced - χ^2	0.03	0.05	0.05	0.09
R_w	0.11	0.16	0.14	0.20

TABLE III. Comparison of the PDF fit quality parameters of pseudo-orthorhombic and tetragonal models of room temperature data within the range $1.8 \text{ \AA} \leq r \leq 20.0 \text{ \AA}$.

$$f_E\left(\frac{\theta_E}{T}\right) = \frac{1}{\exp\left(\frac{\theta_E}{T}\right) - 1} \quad (4)$$

Here, a is the lattice constant, a_0 and c_0 are lattice constants at low temperature (2k for $M = \text{Se}$ and 30 k for $M = \text{S}$ system) obtained from PDF fits, α is the high temperature thermal expansion coefficient, and θ_E is the characteristic Einstein temperature. In our plots, we have used $\theta_E = 211$ K as reported by Free *et al.* [19].

B. Temperature Dependence of Thermal Displacement Parameters

Fig. 5 shows the temperature dependence of the anisotropic thermal displacement parameters U_{11} and U_{33} for both $M = \text{S}, \text{Se}$ from PDF fits. We note the relatively high values of U_{11} parameter for the $M = \text{S}, \text{Se}$ sites and the U_{33} parameter for the O(2) site. The large U_{33} parameter for the O(2) site agrees well with the neutron powder diffraction results (See Table I). The large anisotropic thermal displacement parameter U_{33} corresponds to O(2) displacement above and below the Fe₂O plane. This particular displacement can be accompanied by a distortion of Fe-O-Fe angle (See Fig. 1 where this angle is highlighted by a solid black line in the octahedra). Another possible movement along the c -axis is that of sulfur/selenium atoms with respect to the Fe atoms in the octahedra. This motion would affect the M -Fe- M angle in the octahedra (See Fig. 1 where this angle is highlighted by dashed black lines in the octahedra).

Fig. 6 provides views of the atomic displacements under discussion. Panel a) shows a view along the a -axis while panel b) provides an isometric perspective view by presenting slight rotations about the a and c crystal axes. In panel b) black solid lines show the Fe atom movement

and black dashed line shows the movement of O(2) atom. When the O(2) atoms in the Fe₂O plane move up or down the angle Fe-O-Fe changes causing buckling of the Fe₂O plane. O(2) atoms are displacing out of the plane by ~ 0.015 (2) \AA . Allowing the z -coordinates of the two O(2) atoms to displace opposite to each other results in the U_{33} parameter for the O(2) site dropping down to a value that is in line with other atomic sites. This result suggests that local buckling of the Fe₂O plane may occur through small displacements of the O(2) atom above and below the plane.

C. Local Orthorhombicity

The use of pre-written macros allows PDFGUI to fit data sets through a series of boxcar refinements that differ one from another by corresponding fitting ranges [51]. Since we have collected PDF data sets over a wide range of temperatures, we used PDFGUI T -series and r -series macros to study details of the local to average structure crossover in our materials. These macros allow the setup of boxcar fits, in which the same model is fitted over different real space intervals (r -ranges) for different temperatures of the PDF data [52]. We have performed extensive T - and r -series PDF fits to determine the atomic structure as a function of temperature and length scale [30]. The evolution of the orthorhombicity of the local structure (short-range) to the average structure (long range) is presented in the color maps of Fig. 7. We did the T -series refinement by performing the PDF fits on low temperature data at first, then we run the sequential PDF fits for all of our data collected at various temperatures. For each temperature data, we have performed the r -series refinement in a sliding 20 \AA data window from [1.5 - 21.5 \AA] to [29.5 - 49.5 \AA] in 1 \AA steps, resulting in

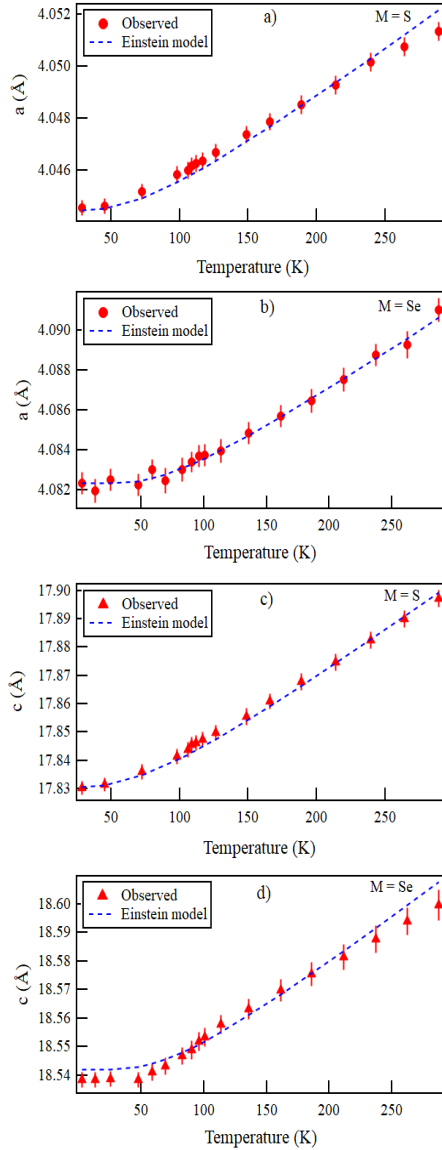


FIG. 4. Lattice parameters as a function of temperature for $M = S, Se$ determined from temperature-series sequential PDF refinement. a) a - and c)-lattice parameter are shown for $M = S$ and b) a - and c)-lattice parameter are shown for $M = Se$. Blue dotted lines represent an Einstein model of lattice thermal expansion (see text).

29 fits per temperature. Orthorhombicity (δ) was extracted from all of these fits for all temperatures to produce the color maps. Color maps were made using the ORIGIN software [53]. In these color maps, the midpoint of the fitting range r_{mid} is shown on the x-axis, the temperature is shown on the y-axis, and orthorhombicity is shown on the color bar as indicated by the brightness of the colors from light blue to dark blue. The dark blue color denotes high orthorhombicity, light blue represent zero orthorhombicity *i.e.*, tetragonality. The maps indicate that at short ranges, over all temperatures, the presence of orthorhombicity is observed, but it dimin-

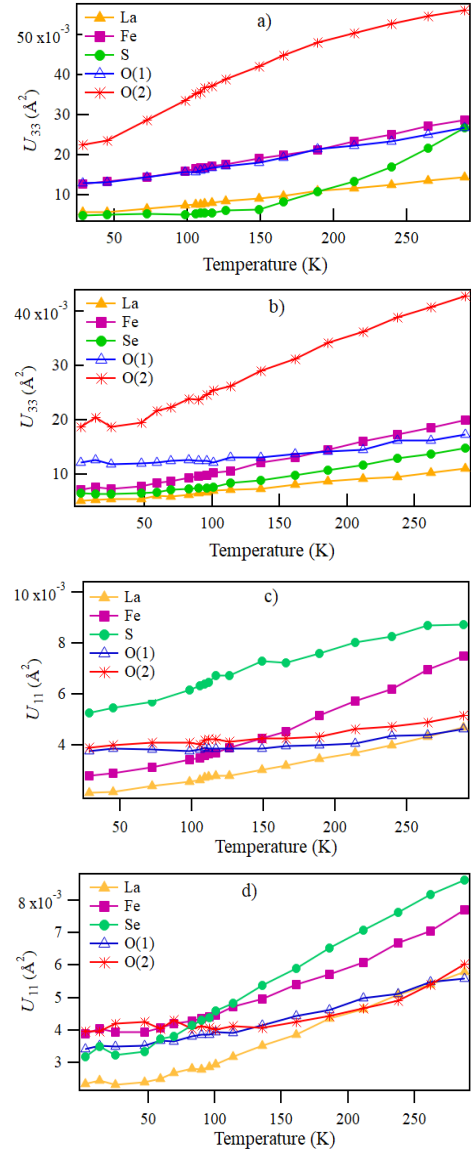


FIG. 5. The temperature dependence of the anisotropic thermal displacement parameters a) U_{33} and c) U_{11} for $M = S$; and b) U_{33} and d) U_{11} for $M = Se$ for all atomic sites determined from temperature-series sequential PDF refinement within the range $1.8 \text{ \AA} \leq r \leq 20.0 \text{ \AA}$.

ishes over longer length scales. Fig. 7(c) shows the temperature dependence of short-range orthorhombicity for $La_2O_2Fe_2O(S, Se)_2$. It was observed that orthorhombicity is independent of temperature below ~ 150 K and at higher temperatures, orthorhombicity decreases slightly with temperature.

Fig. 8 presents the local orthorhombicity δ as a function of the midpoint of the fitting ranges for two representative temperatures. Data were fitted with exponential decay functions,

$$f(x) = A_1 \exp\left(\frac{-x}{t_1}\right) + Constant \quad (5)$$

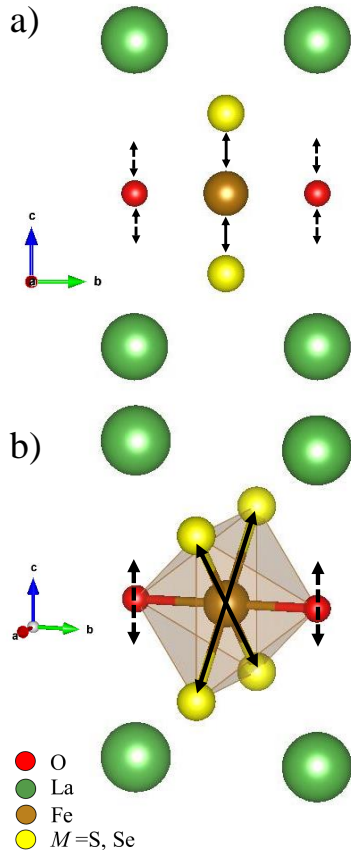


FIG. 6. Panel (a) shows possible Fe and Se/S atomic movement within the $\text{La}_2\text{O}_2\text{Fe}_2\text{O}(\text{S, Se})_2$ octahedra that result in the bucking of the Fe_2O plane. (b) The dashed lines show Fe atom movement in the Fe_2O plane and the solid lines show Fe movement with respect to M .

where decay length is defined as $\ln 2 \times t_1$.

Fig. 8(a) shows the orthorhombicity of $M = \text{S}$ at 28.45 K and 214.0 K. At both temperatures, the orthorhombicity is largest at short fitting ranges and it asymptotically approaches zero at larger fitting ranges. A black solid (dashed) line shows the exponential fitting function for 28.45 K (214.0 K) with decay lengths of 6.4(2) \AA (3.5(9) \AA), respectively. Fig. 8(b) displays the orthorhombicity at different fitting ranges for $M = \text{Se}$ at temperature 2.57 K and 211.47 K. Black solid (dashed) line shows the exponential fitting function for 2.57 K (211.47 K) with decay length of 7.5(3) \AA (7.9(6) \AA), respectively. Figs. 8(a) and (b) provide evidence of the greater orthorhombicity at shorter ranges.

IV. DISCUSSION

Neutron powder diffraction experiments confirmed the average crystal structure of $\text{La}_2\text{O}_2\text{Fe}_2\text{O}(\text{S, Se})_2$ as tetragonal systems with space group ($I4/mmm$) (see Fig. 2)

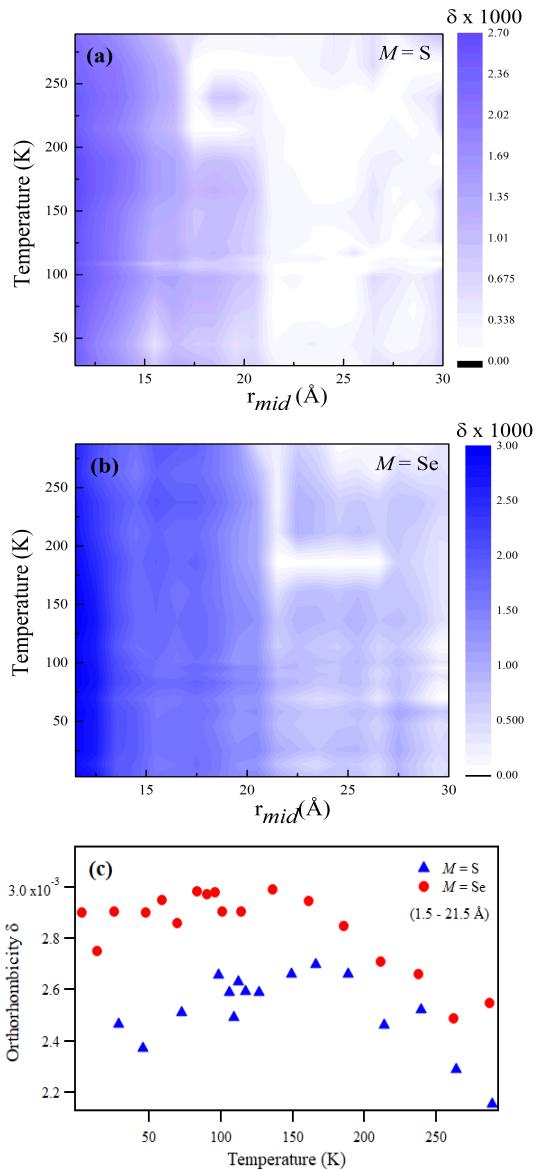


FIG. 7. Color maps of the refined orthorhombicity determined from neutron PDF analysis for a) $M = \text{S}$ and b) $M = \text{Se}$. c) Temperature dependence of short-range (1.5 - 21.5 \AA) orthorhombicity.

in agreement with the previous studies on these materials [12, 15–19]. Unlike many iron pnictides which undergo a structural phase transition from tetragonal to orthorhombic symmetries near T_s , $\text{La}_2\text{O}_2\text{Fe}_2\text{O}(\text{S, Se})_2$ lattice symmetries are not observed to change with temperature. However, both $\text{La}_2\text{O}_2\text{Fe}_2\text{O}(\text{S, Se})_2$ undergo a magnetic transitions from paramagnetic (PM) phases to antiferromagnetic (AFM) phases at respective Néel temperatures T_N . Neutron powder diffraction (Fig. 5 and Table I) showed that the thermal displacement parameter for the O(2) atom along the c -axis was larger than all the other thermal displacement parameters. This was the finding for both materials $M = \text{S}$ and Se.

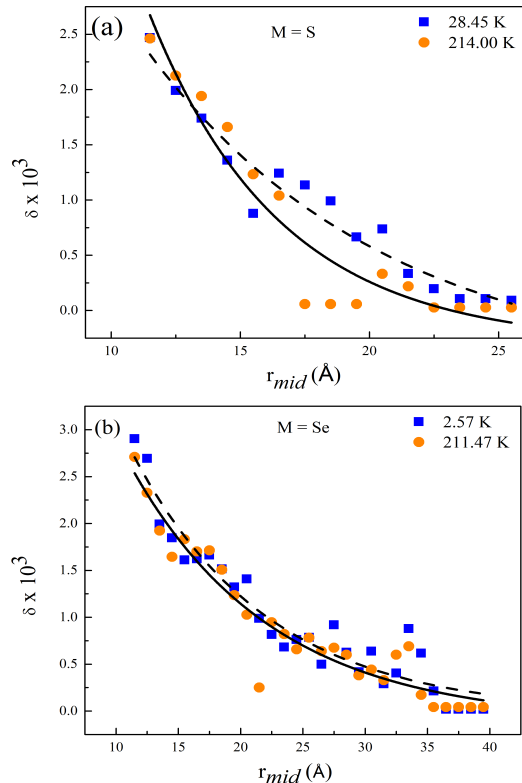


FIG. 8. Orthorhombicity as a function of fitting range for a) $M = S$ and b) $M = Se$ at low and high temperature.

In order to probe the local structure, we employed the neutron PDF technique to investigate the local changes in the atomic positions and c -axes of $La_2O_2Fe_2O(S, Se)_2$. The PDF analysis revealed similar thermal displacement behavior on short length scales. In addition, the temperature dependence of the c -lattice parameter showed a kink near the Néel temperature for $M = Se$ (see Fig. 4). However, no discontinuity was observed in the case of $M = S$. Such a finding is consistent with previous reports of c -lattice discontinuities in oxyselenides [19, 54, 55] and the less prominent occurrence of this behavior in the oxysulfides [18]. The discontinuities were attributed to magnetostrictive effects in the oxyselenides. In the case of oxysulfides, a relatively reduced amount of c -lattice discontinuity was argued to be due to shorter c -lattices [18]. According to Horigane et al. [40] deviations in the c -lattice parameter from the average crystallographic structure are due to the fact that the thermal displacement parameter U_{33} for O(2) along the c -axis grows rapidly with the increase in temperature. A similar O(2) trend, in $SrFeO_2$ [56], was reported to be related to Fe_2O planar buckling.

For $La_2O_2Fe_2O(S, Se)_2$, buckling of the Fe_2O plane may occur when there is distortion in either the Fe or O(2) sites. In the case of $M = Se$, a high U_{33} value for O(2) (see Fig. 5) suggests that the largest distortions should occur for that site. A distortion in the Fe site

can lead to two Fe-Se correlations since each Fe atom is surrounded by four Se atoms of the octahedra (see Fig. 6b). Overall, these findings for $M = Se$ suggest that there is a distortion either in the Fe or O(2) sites, and both implicated as possible reasons for Fe_2O buckling.

Our analysis of the local structure of $La_2O_2Fe_2O(S, Se)_2$ reveals the presence of short-range orthorhombic distortions on a length scale of 1 - 2 nm over a temperature range from 2 - 300 K. These distortions are very similar to those found in FeSe [34, 38] and $(Sr, Na)Fe_2As_2$ [30, 31], which have been attributed to short-range, structural nematic fluctuations that persist up to temperatures well above the magnetic and/or structural transition temperatures. Given the structural and magnetic similarities between these iron oxychalcogenides and the superconducting iron pnictides and chalcogenides, we suggest that the local orthorhombicity observed here is likewise related to fluctuating, short-range electronic nematic distortions. The short-range orthorhombicity observed up to high temperature (~ 300 K) in these systems may reflect a similar large nematic energy scale as was observed in FeSCs such as FeSe [57] and $(Sr, Na)Fe_2As_2$ [38].

The occurrence of such distortions across a variety of pnictide superconductors and the incoherent electronic systems presented here raise the question of how are these short-range orthorhombic distortions related to the superconducting mechanism. Inquiry into the role of *electronic* nematicity has become the key focal point of the field of iron-based high- T_c superconductivity. Studies of short-range orthorhombic fluctuations, such as those reported here, may provide information about the origin of electronic nematicity and its relation to superconductivity mechanism [34, 38, 58–63].

The presence of local orthorhombicity that appears to be ubiquitous may be suggestive of nematic degrees of freedom being ubiquitously active in layered iron-based systems. It also suggests that active nematic degrees of freedom are not sufficient to guarantee superconductivity, although they may well be necessary. It may be the case that nematic fluctuations and another phase must conspire to produce high-temperature superconductivity in iron-based systems. The energy-integrated nature of the PDF measurements means we are probing fluctuations on a time scale of 10^{-13} s or slower. However, we were unable to extract any other temporal information using the PDF data alone [31]. Complementary probes such as NMR or Mössbauer spectroscopy could help clarify the situation [64].

V. CONCLUSIONS

The local structure of Mott insulating iron oxychalcogenides was studied using neutron powder diffraction and pair distribution techniques. Neutron powder diffraction showed a similar nuclear structure of $M = Se$ and S with the only difference in the atomic radii of two chalcogens. Pair distribution function analysis indicated the presence

of the local distortion between tetragonal and orthorhombic symmetry. These findings suggest the presence of orthorhombic fluctuations suggestive of short-range nematicity with a typical length scale of 1 - 2 nm in both of these materials.

VI. ACKNOWLEDGMENTS

The authors would like to thank the University of Louisville for funding support. Alfailakawi would like to thank Kuwait University for supporting this work

through a graduate scholarship. Work at University of Houston was supported by the State of Texas through TcSUH. The research in ZJU is supported by the Ministry of Science and Technology of China under Grants No. 2016YFA0300402 and No. 2015CB921004 and the National Natural Science Foundation of China (NSFC) (No. 11974095, 11374261), and the Fundamental Research Funds for the Central Universities. This work used resources of the Spallation Neutron Source, a DOE office of Science User Facility operated by the Oak Ridge National Laboratory.

-
- [1] Q. Si, R. Yu, and E. Abrahams, *Nature Reviews Materials* **1**, 16017 (2016).
- [2] J. Paglione and R. L. Greene, *Nature Physics* **6**, 645 (2010).
- [3] L. Zhao, D. Wang, Q. Huang, H. Wu, R. Sun, X. Fan, Y. Song, S. Jin, and X. Chen, *Physical Review B* **99**, 094503 (2019).
- [4] T. Yildirim, *Phys. Rev. Lett.* **102**, 037003 (2009).
- [5] Q. Si and E. Abrahams, *Phys. Rev. Lett.* **101**, 076401 (2008).
- [6] B. Mansart, D. Boschetto, A. Savoia, F. Rullier-Albenque, F. Bouquet, E. Papalazarou, A. Forget, D. Colson, A. Rousse, and M. Marsi, *Phys. Rev. B* **82**, 024513 (2010).
- [7] S. Lee, S. Roh, Y.-S. Seo, M. Lee, E. Jung, J. M. Ok, M.-C. Jung, B. Kang, K.-W. Lee, J. S. Kim, *et al.*, *Journal of Physics: Condensed Matter* **31**, 445602 (2019).
- [8] C. H. Wong and R. Lortz, *arXiv preprint arXiv:1902.06463* (2019).
- [9] E. Abrahams and Q. Si, *Journal of physics: Condensed matter* **23**, 223201 (2011).
- [10] S. K. Shrivastava and G. Kumar, *International Journal of Emerging Technologies and Innovative Research* **6**, 417 (2019).
- [11] S. Landsgesell, K. Prokeš, T. Hansen, and M. Frontzek, *Acta Materialia* **66**, 232 (2014).
- [12] J.-X. Zhu, R. Yu, H. Wang, L. L. Zhao, M. D. Jones, J. Dai, E. Abrahams, E. Morosan, M. Fang, and Q. Si, *Phys. Rev. Lett.* **104**, 216405 (2010).
- [13] P. A. Lee, N. Nagaosa, and X.-G. Wen, *Rev. Mod. Phys.* **78**, 17 (2006).
- [14] M. H. Fischer, S. Wu, M. Lawler, A. Paramakanti, and E.-A. Kim, *New Journal of Physics* **16**, 093057 (2014).
- [15] J. M. Mayer, L. F. Schneemeyer, T. Siegrist, J. V. Waszczak, and B. Van Dover, *Angewandte Chemie International Edition in English* **31**, 1645 (1992).
- [16] B. Freelon, Z. Yamani, I. Swainson, R. Flacau, B. Karki, Y. H. Liu, L. Craco, M. S. Laad, M. Wang, J. Chen, R. J. Birgeneau, and M. Fang, *Phys. Rev. B* **99**, 024109 (2019).
- [17] E. E. McCabe, C. Stock, E. E. Rodriguez, A. S. Wills, J. W. Taylor, and J. S. O. Evans, *Phys. Rev. B* **89**, 100402(R) (2014).
- [18] R. K. Oogarah, E. Suard, and E. E. McCabe, *Journal of Magnetism and Magnetic Materials* **446**, 101 (2018).
- [19] D. G. Free and J. S. O. Evans, *Phys. Rev. B* **81**, 214433 (2010).
- [20] L. Craco, B. Freelon, A. M. Alfailakawi, B. Karki, and S. Leoni, *Phys. Rev. B* **98**, 045130 (2018).
- [21] C. Stock and E. E. McCabe, *Journal of Physics: Condensed Matter* **28**, 453001 (2016).
- [22] M. Günther, S. Kamusella, R. Sarkar, T. Goltz, H. Luetkens, G. Pascua, S.-H. Do, K.-Y. Choi, H. D. Zhou, C. G. F. Blum, S. Wurmehl, B. Büchner, and H.-H. Klauss, *Phys. Rev. B* **90**, 184408 (2014).
- [23] P. Dai, J. Hu, and E. Dagotto, *Nature Physics* **8**, 709 (2012).
- [24] R. M. Fernandes, A. V. Chubukov, and J. Schmalian, *Nature Physics* **10**, 97 (2014).
- [25] J.-H. Chu, H.-H. Kuo, J. G. Analytis, and I. R. Fisher, *Science* **337**, 710 (2012).
- [26] J. Li, P. J. Pereira, J. Yuan, Y.-Y. Lv, M.-P. Jiang, D. Lu, Z.-Q. Lin, Y.-J. Liu, J.-F. Wang, L. Li, *et al.*, *Nature communications* **8**, 1880 (2017).
- [27] R. M. Fernandes and A. J. Millis, *Physical review letters* **111**, 127001 (2013).
- [28] E. Fradkin, S. A. Kivelson, M. J. Lawler, J. P. Eisenstein, and A. P. Mackenzie, *Annu. Rev. Condens. Matter Phys.* **1**, 153 (2010).
- [29] A. V. Chubukov, R. M. Fernandes, and J. Schmalian, *Physical Review B* **91**, 201105(R) (2015).
- [30] B. A. Frandsen, K. M. Taddei, D. E. Bugaris, R. Stadel, M. Yi, A. Acharya, R. Osborn, S. Rosenkranz, O. Chmaissem, and R. J. Birgeneau, *Phys. Rev. B* **98**, 180505(R) (2018).
- [31] B. A. Frandsen, K. M. Taddei, M. Yi, A. Frano, Z. Guguchia, R. Yu, Q. Si, D. E. Bugaris, R. Stadel, R. Osborn, S. Rosenkranz, O. Chmaissem, and R. J. Birgeneau, *Phys. Rev. Lett.* **119**, 187001 (2017).
- [32] S. Okamoto, D. Sénéchal, M. Civelli, and A.-M. S. Tremblay, *Phys. Rev. B* **82**, 180511(R) (2010).
- [33] Y. Kushnirenko, D. Evtushinsky, T. Kim, I. Morozov, L. Harnagea, S. Wurmehl, S. Aswartham, A. Chubukov, and S. Borisenko, *arXiv preprint arXiv:1810.04446* (2018).
- [34] R. J. Koch, T. Konstantinova, M. Abeykoon, A. Wang, C. Petrovic, Y. Zhu, E. S. Bozin, and S. J. L. Billinge, *Phys. Rev. B* **100**, 020501(R) (2019).
- [35] C. M. Yim, C. Trainer, R. Aluru, S. Chi, W. N. Hardy, R. Liang, D. Bonn, and P. Wahl, *Nature Communications* **9**, 2602 (2018).

- [36] T. Egami and S. J. L. Billinge, *Underneath the Bragg Peaks: Structural Analysis of Complex Materials* (Pergamon Press Elsevier, Oxford, England, 2003).
- [37] C. L. Farrow, P. Juhas, J. W. Liu, D. Bryndin, E. S. Božin, J. Bloch, T. Proffen, and S. J. L. Billinge, *Journal of Physics: Condensed Matter* **19**, 335219 (2007).
- [38] B. A. Frandsen, Q. Wang, S. Wu, J. Zhao, and R. J. Birgeneau, *Phys. Rev. B* **100**, 020504(R) (2019).
- [39] D. Louca, K. Horigane, A. Llobet, R. Arita, S. Ji, N. Katayama, S. Konbu, K. Nakamura, T.-Y. Koo, P. Tong, and K. Yamada, *Phys. Rev. B* **81**, 134524 (2010).
- [40] K. Horigane, K. Kawashima, S. Ji, M. Yoshikawa, D. Louca, and J. Akimitsu, in *Proceedings of the International Conference on Strongly Correlated Electron Systems (SCES2013)* (2014) p. 015039.
- [41] B. H. Toby and R. B. Von Dreele, *Journal of Applied Crystallography* **46**, 544 (2013).
- [42] P. Juhás, J. N. Louwen, L. van Eijck, E. T. C. Vogt, and S. J. L. Billinge, *Journal of Applied Crystallography* **51**, 1492 (2018).
- [43] T. Proffen and S. J. L. Billinge, *Journal of Applied Crystallography* **32**, 572 (1999).
- [44] C. E. White, J. L. Provis, T. Proffen, and J. S. Van Deventer, *Journal of the American Ceramic Society* **93**, 3486 (2010).
- [45] M. Paściak, P. Ondrejko, J. Kulda, P. Vaněk, J. Drahoš, G. Steciuk, L. Palatinus, T. R. Welberry, H. E. Fischer, J. Hlinka, and E. Buixaderas, *Physical Review B* **99**, 104102 (2019).
- [46] W. A. Slawinski, H. Y. Playford, S. Hull, S. T. Norberg, S. G. Eriksson, T. Gustafsson, K. Edstrom, and W. R. Brant, *Chemistry of Materials* **31**, 5024 (2019).
- [47] I.-K. Jeong and B.-G. Kim, *Journal of Applied Physics* **126**, 014101 (2019).
- [48] A. S. Masadeh, E. S. Božin, C. L. Farrow, G. Paglia, P. Juhas, S. J. L. Billinge, A. Karkamkar, and M. G. Kanatzidis, *Physical Review B* **76**, 115413 (2007).
- [49] B. Toby and T. Egami, *Acta Crystallographica Section A: Foundations of Crystallography* **48**, 336 (1992).
- [50] H. Kröncke, S. Figge, D. Hommel, and B. M. Epelbaum, *Acta Phys. Pol. A* **114**, 1193 (2008).
- [51] C. Farrow, P. Juhas, J. Liu, D. Bryndin, E. Božin, J. Bloch, T. Proffen, and S. Billinge, *Journal of Physics: Condensed Matter* **19**, 335219 (2007).
- [52] A. M. Abeykoon, W. Donner, M. Brunelli, M. Castro-Colin, A. J. Jacobson, and S. C. Moss, *Journal of the American Chemical Society* **131**, 13230 (2009).
- [53] OriginPro 2013, *OriginLab Corporation*, Northampton, MA, USA.
- [54] E. E. McCabe, A. S. Wills, L. Chapon, P. Manuel, and J. S. O. Evans, *Phys. Rev. B* **90**, 165111 (2014).
- [55] R. K. Oogarah, C. P. J. Stockdale, C. Stock, J. S. O. Evans, A. S. Wills, J. W. Taylor, and E. E. McCabe, *Phys. Rev. B* **95**, 174441 (2017).
- [56] K. Horigane, A. Llobet, and D. Louca, *Phys. Rev. Lett.* **112**, 097001 (2014).
- [57] M. Yi, H. Pfau, Y. Zhang, Y. He, H. Wu, T. Chen, Z. R. Ye, M. Hashimoto, R. Yu, Q. Si, D.-H. Lee, P. Dai, Z.-X. Shen, D. H. Lu, and R. J. Birgeneau, *Phys. Rev. X* **9**, 041049 (2019).
- [58] H.-H. Kuo, J.-H. Chu, J. C. Palmstrom, S. A. Kivelson, and I. R. Fisher, *Science* **352**, 958 (2016).
- [59] A. E. Böhmer and C. Meingast, *Comptes Rendus Physique* **17**, 90 (2016).
- [60] E. P. Rosenthal, E. F. Andrade, C. J. Arguello, R. M. Fernandes, L. Y. Xing, X. C. Wang, C. Q. Jin, A. J. Millis, and A. N. Pasupathy, *Nature Physics* **10**, 225 (2014).
- [61] J. Wang, G.-Z. Liu, D. V. Efremov, and J. van den Brink, *Phys. Rev. B* **95**, 024511 (2017).
- [62] P. Dai, *Rev. Mod. Phys.* **87**, 855 (2015).
- [63] G. R. Stewart, *Rev. Mod. Phys.* **83**, 1589 (2011).
- [64] B. Freelon, R. Sarkar, S. Kamusella, F. Brückner, V. Grinenko, S. Acharya, M. Laad, L. Craco, Z. Yamani, R. Flacau, I. Swainson, B. Frandsen, R. Birgeneau, Y. Liu, B. Karki, A. Alfailakawi, J. C. Neufeind, M. Everett, H. Wang, B. Xu, M. Fang, and H.-H. Klauss, *npj Quantum Materials* **6**, 4 (2021).